npj | materials degradation

Article

Published in partnership with CSCP and USTB

https://doi.org/10.1038/s41529-024-00464-8

Metastable cellular structures govern localized corrosion damage development in additive manufactured stainless steel

Evan DelVecchio[1], Tiffany Liu[1], Yen-Ting Chang[1], Yuheng Nie[1], Maryam Eslami[2] & Marie A. Charpagne[1]

The rapid solidification associated with additive manufacturing (AM) leads to complex microstructures with peculiar features amongst which cellular solidification structures are the most remarkable. These metastable structures possess a clear segregation pattern dictated by the solidification pathway of the alloy and are bounded by dislocation walls. While they confer exceptional strength and ductility to AM 316L stainless steel, their effect on localized corrosion in chloride environments remains to be established. Here, we employ correlative electron microscopy to reveal coupled chemical, electrochemical, and crystallographic effects on localized corrosion attack and its development. We show that the Cr and Mo-depleted interior of the cellular solidification structures dissolves selectively, giving rise to an intricate damage morphology, that is directly related to the underlying crystallographic orientation. Whereas surface observations only reveal apparently shallow micrometer-size cavities, 3D tomography via focused ion beam serial-sectioning shows a high degree of connectivity between these features underneath the surface. We reveal this intricate morphology, propose a formation mechanism, and discuss alloy design guidelines to mitigate this phenomenon.

316L stainless steel is a material of choice for a broad array of structural applications due to its high toughness, formability, creep resistance, and resistance to chloride-containing environments. Readily printable via laser additive manufacturing (AM), including laser powder bed fusion (LPBF) and direct energy deposition (DED), 316L is the most studied AM alloy as of today. The thermal-mechanical cycling that arises from the layer-by-layer deposition process gives rise to an intricate and multi-scale microstructure. It is still controversial if the change in microstructure leads to favorable corrosion performance, specifically in terms of passive film stability[1,2]. This controversy extends beyond aqueous NaCl environments into more acidic mediums such as HCl[3,4]. The AM microstructure is characterized by elongated grains which ⟨001⟩ crystallographic direction follows the steepest temperature gradient during solidification. Those grains typically exhibit cellular sub-structures, characteristic of rapidly solidified alloys[5], referred to as cells in the following. Cells are bounded by dislocation arrays and are enriched in Cr, Mo, and Ni as a result of rapid austenite-to-ferrite solidification[6,7]. Their role in the development of localized corrosion is still subject to debate until now. While Cr and Mo enrichment would theoretically increase the local corrosion resistance[6], leading to a thicker and more stable passive layer, cell walls have been observed to exhibit faster corrosion than cell interiors in several instances[8]. This was attributed to Mn-containing nano-scale silicates, located within the cell walls, that form due to rapid oxidation during AM[8,9]. Despite a typically lower, hence more active electrochemical potential[6], the cell interiors usually contain dislocations with a typical density of 10^{14} m^{-2} in laser powder bed fusion (LPBF) and 10^{13} m^{-2} in direct energy deposition (DED)[5], which was postulated to increase the stability of the passive film[1,10,11]. Whereas dedicated studies have been published in the past 6 years[10,12,13], there is still no consensus on how the microstructure features that are unique to AM materials affect corrosion damage development[14].

The conflicting phenomena detailed above suggest that corrosion attack and its development would depend on the local microstructure and the local composition, dislocation density, and second-phases, which themselves vary with printing parameters. Most studies have focused on the parameters related to the stability of the passive film, including pitting and repassivation potentials, complemented by optical microscopy. These have revealed evidence of localized corrosion occurring under the form of pits with a "geometric morphology", which are challenging to repassivate[1]. On the other hand, nano-scale characterization techniques, such as in situ transmission electron microscopy (TEM) and atomic force microscopy

[1]Department of Materials Science and Engineering, University of Illinois Urbana-Champaign, Urbana, IL 61801, USA. [2]Illinois Applied Research Institute, University of Illinois Urbana-Champaign, Champaign, IL 61820, USA. e-mail: mcharp@illinois.edu

(AFM), have been instrumental in revealing the incipient stages of localized corrosion[8,14]. These have revealed micro-galvanic effects at cell boundaries and preferential dissolution of the cell walls, which does not corroborate with the pit morphology observed in macroscopic studies. This may stem from the fact that these techniques can only probe free surfaces (AFM) and thin specimens (TEM), where surface effects are emphasized.

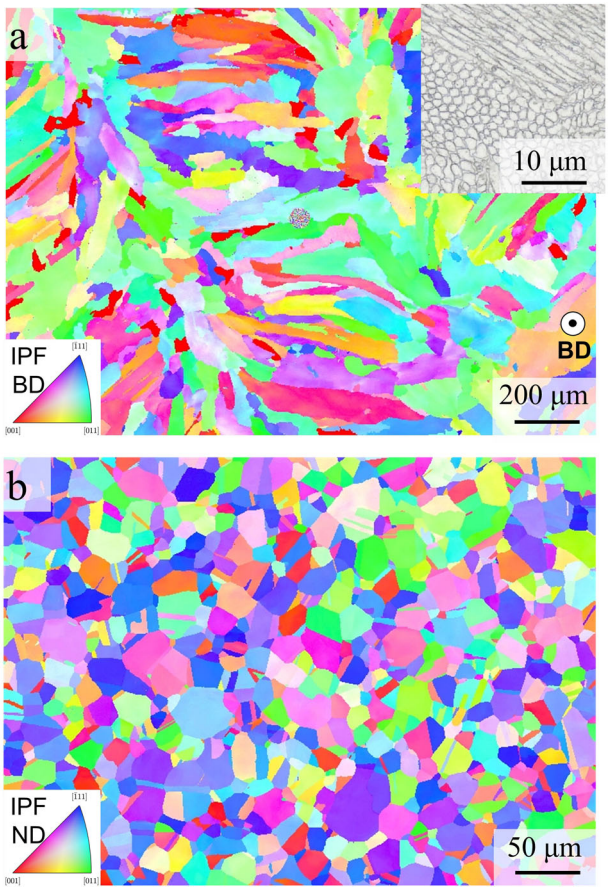

Fig. 1 | Microstructure of the two materials studied. EBSD orientation maps of (**a**) AM 316L and (**b**) recrystallized 316L in IPF colors with respect to the normal direction to the observation plane. The insert in (**a**) shows the sub-grain cellular structures after etching with $FeCl_3$, $CuCl_2$, highlighting systematic elemental segregation at the cell walls.

To summarize, the micro/nano-scale effects reported so far do not corroborate with the pit morphology observed at the macro-scale. While many studies have focused on the stability of the passive film, there is little knowledge about the mechanisms of localized corrosion in AM stainless steels.

To fill this knowledge gap, we carry out a multi-scale and three-dimensional investigation of corrosion attack in DED AM 316L, focusing on its linkage with the underlying microstructure. By means of correlative electron microscopy, we probe coupled chemical and crystallographic effects on damage development and reveal that the cellular solidification structures, unique to AM stainless steels, guide the growth of localized corrosion. This leads to corrosion damage sites with unique and intricate tubular morphology, which principal orientation depends strongly on the underlying crystallographic orientation, a feature never observed in wrought alloys. We propose a mechanism for the formation of these localized corrosion sites, and discuss their implication in the context of alloy design for AM.

Results

As-built and recrystallized microstructures

Figure 1a, b shows electron back-scatter diffraction (EBSD) maps of the AM and recrystallized microstructures, respectively, in inverse pole figure (IPF) colors with respect to the normal direction to the observation plane. This direction corresponds to the build direction (BD) for the AM material and the normal direction for the wrought sample. AM 316L exhibits long columnar grains that align with the laser raster pattern, measuring 90 µm on average and a few keyhole-type defects (with a typical density of 10 per cm^2), likely due to stochastic variations in local processing parameters. One of such keyholes is visible in the center of Fig. 1a. On the other hand, the annealed sample exhibits equiaxed grains with random texture and annealing twins, which is typical of fully recrystallized microstructures. Its average grain size is 31 µm.

Electrochemical behavior and corrosion attack morphology

The anodic polarization curves of the two materials studied are shown in Fig. 2a. Both materials show a clear passive behavior with similar passive current density in the range of 10^{-6} to 10^{-7} A/cm^2 with the AM material having a slightly lower passive current value. The passive region is relatively wider and is about 0.7 V for the AM material. With respective values of 585.8 mV and 510.6 mV, averaged over five samples in each material, the AM material exhibits a higher breakdown potential than its recrystallized counterpart, as summarized in Table 1. The clear difference between the breakdown potentials of the two materials shows that a higher driving force is needed to initiate pitting in the AM sample. This difference in breakdown potential has been previously observed and reported under different corrosion

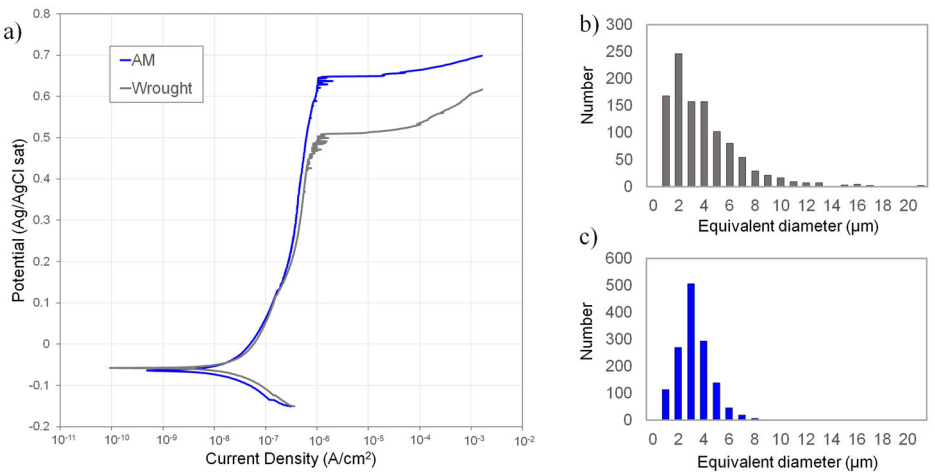

Fig. 2 | Electrochemical behavior and corrosion damage. a Potentiodynamic polarization (PDP) curves for AM 316L (blue) and recrystallized 316L (gray), size distribution of localized corrosion damage sites in (**b**) recrystallized 316L, (**c**) AM 316L.

Table 1 | Average breakdown potential and localized damage size distribution in the recrystallized and AM materials

Material	Breakdown potential (vs. Ag/AgCl)	Average pit size
Recrystallized	510.6 ± 14 mV	3.58 µm
AM	585.8 ± 34 mV	2.75 µm (67.6 µm, clusters)

conditions[15–17]. It could be due to the absence of MnS inclusions in the wrought material and the associated Cr-depletion zones surrounding them[18], that largely contribute to pitting initiation in wrought stainless steels[19]. Another explanation for the difference in pitting potential of the two materials can be borrowed from studies on the passive oxide layers formed on LPBF and wrought 316L alloys, where thicker passive films (1.2 to 1.5 times thicker) have been detected on the LPBF alloys exposed to borate buffer solution and simulated body fluid[15,20]. Based on this, we can anticipate a better performance from the AM alloy in other environments, but this requires dedicated additional investigations. Interestingly, only a few current spikes are observed prior to reaching the breakdown potential. Spikes are commonly observed and associated with the occurrence of metastable pitting[12]. Together, these results indicate that the passive film is stable in a wide range of potentials in both materials.

Corrosion damage was characterized via optical microscopy after potentiodynamic polarization (PDP). Both materials exhibit localized forms of corrosion, yet with distinct size and morphology. Figure 2b, c shows the size distribution of damage sites in the recrystallized and AM samples, respectively. While both size distributions are centered around 2 µm, the pits in the recrystallized 316L cover a wider range of sizes, in accordance with the earlier breakdown of the passive film observed in this material. Interestingly, despite its higher breakdown potential, AM 316L shows a very narrow size distribution with many localized corrosion features in the range of 2–5 µm, with an approximate count of 800 per cm^2. This tight size distribution depicts a consistent and characteristic length scale in the localized corrosion of the AM material, which is indicative of a common feature across the AM samples. On the opposite, the wrought sample exhibits a broader size distribution, in accordance with a typical pitting corrosion behavior. Together, these results could refer to a specific microstructural feature playing a role in the localized corrosion of the AM material.

To link the localized corrosion damage with the underlying microstructure, the surface of the specimens was characterized using correlative electron microscopy, coupling scanning electron microscopy (SEM) and EBSD. As shown in the SEM images in Fig. 3, localized corrosion exhibits a typical pitting morphology in the recrystallized material. The pits are in the form of individual cavities that develop on the surface, globular in shape, with an equivalent diameter of 3.58 µm on average (summarized in Table 1). Figure 3 shows two representative examples of such pits, with contrasting sizes. Individual pits span across several grains in width and depth, as revealed by the apparent grain boundary traces in Fig. 3a. While the roughness of the edge of the pits varies for both early-stage and developed pits (Fig. 3b), there is no apparent correlation between the grain structure and the pit shape, in agreement with previous literature[21,22].

The AM material also exhibits highly localized corrosion damage, but with a drastically different morphology compared to its recrystallized counterpart. A representative example is presented in Fig. 4a. All localized corrosion sites systematically contain a network of elliptical cavities with average size of 2.75 µm, clustered together into larger features with an average size of 67.6 µm, as summarized in Table 1. Unlike the typical pitting morphology observed in the wrought alloy, corrosion damage is indicative of a form of selective dissolution in AM 316L, i.e. localized corrosion driven by microstructural features with contrasting corrosion resistance. A similar morphology has been shown in stainless steels synthesized using other AM processes, all involving rapid solidification[1,2,23], but it has not been explained or investigated in detail. Interestingly, the corrosion damage site shown in Fig. 4a presents two regions, where the cavities are collectively aligned along a specific direction, as indicated by the darker contrast in the SEM images. A

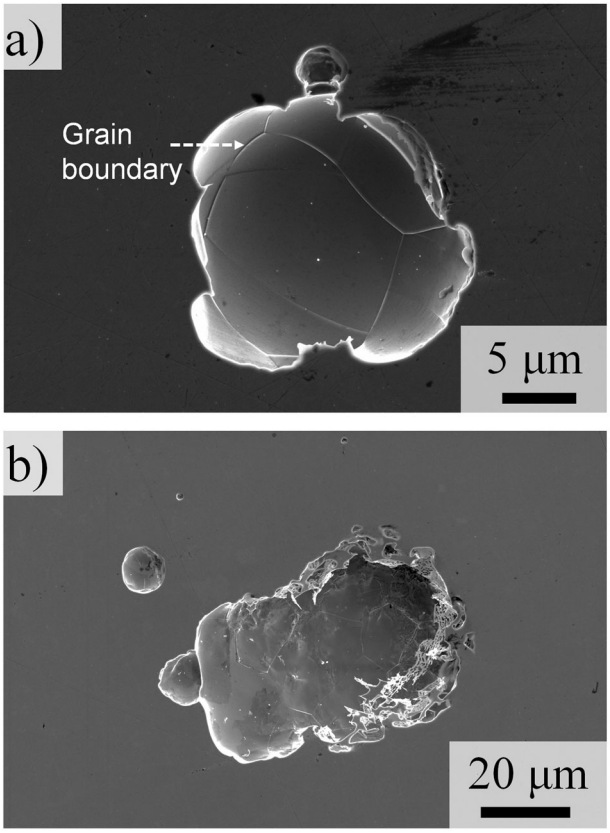

Fig. 3 | Corrosion pits in recrystallized 316L. a Rounded pit spanning across multiple grain boundaries, **b** Fully grown elongated pit with rugged edges.

high magnification SEM image of the purple box region in Fig. 4a is shown in Fig. 4b. The cavities are evenly spaced and exhibit rugged contours. Backscattered electron (BSE) images collected at the rim of the damage site, shown in Fig. 4c, reveal that the cavities align with the local microsegregation pattern, and clearly correspond to the cell structures[5,6].

Cell structures are typically formed under the combination of moderate to high ratios between temperature gradient and crystal growth rate. Their three-dimensional structure is tubular in shape, with a high aspect ratio[24]. The long axis of these cellular structures corresponds to a ⟨001⟩ direction, the fastest growing crystal direction in face centered cubic (fcc) alloys[25]. On free surfaces, depending on the cross-section direction, cells exhibit an apparent topology ranging from circular to elliptical. Together, these results suggest that the corrosion damage would depend on the underlying crystallographic orientation. To probe this dependence, we employ multi-modal electron microscopy techniques at the sub-cell scale, combining compositional and orientation mapping.

Crystallographic-dependence of corrosion damage

EBSD datasets were collected around localized corrosion sites. A representative example is shown in Fig. 5. The IPF-colored orientation map shown in Fig. 5a shows that the localized corrosion site spans across a high-angle grain boundary. The orientation of the cubic lattice is sketched within each grain. Comparison with the corresponding SEM image in Fig. 5b reveals that the cavities grew along a single ⟨001⟩ direction, which is highlighted in bold red on the lattice symbols in Fig. 5a. This indicates that the 3D structure of the solidification cells directly affects the corrosion damage morphology and its development.

3D characterization of localized corrosion

FIB cross-sections collected across the corrosion site reveal a strong directionality in the cavities sub-surface structure, resulting in a drastic orientation difference across the grain boundary. The traces of the two ⟨001⟩

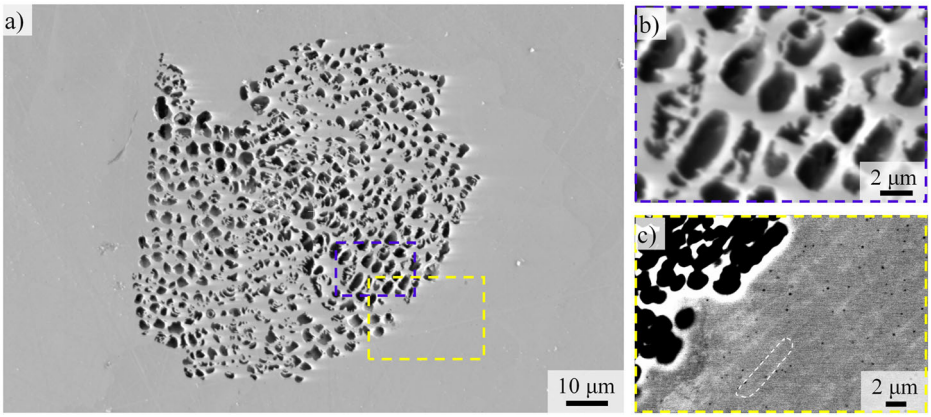

Fig. 4 | Representative corrosion morphology in the AM material after polarization tests up to 10^{-3} A/cm². **a** Overview of the site showing multiple individual cavities, elliptical in shape, clustered together into a large region, **b** high magnification SEM image of the region highlighted in purple in (**a**), showing the morphology of individual cavities, **c** high resolution BSE image of the region highlighted in yellow in (**a**), showing alignment of the cavities with the cellular solidification structures.

crystallographic directions that align with the cells longest axis are highlighted in Fig. 5c. Beyond the striking crystallographic dependence of the damage, which is traditionally not observed in wrought materials, this cross-section reveals the depth of the damage as well as the intricate 3D structure underneath the surface. Finally, the FIB cross-section reveals that the cavities are seemingly connected to one another in the bulk, through small junctions across the grain boundary.

To study the 3D structure and connectivity of the damage, FIB serial sectioning with SEM imaging were carried out throughout the entire localized corrosion site shown in Fig. 5. The serial sectioning sequence is shown in Supplementary Material A. Each SEM image was segmented, highlighting the contours of individual cavities. One example is shown in Supplementary Material B. The segmented cavities were colored according to the local orientation before image stacking and alignment. The reconstructed 3D dataset is shown in Fig. 6, with grains 1 and 2 from Fig. 5 labeled. The dimensions of the damage site are surprisingly large: 154 μm (length) × 52 μm (width) × 49 μm (depth). Individual cavities are bundled together in each grain with clear directionality following the local cell structure, as shown in Fig. 6b. Unlike surface observations and single FIB cross-section, the 3D dataset reveals a high degree of connectivity between the cavities underneath the surface including through the grain boundary, as shown in Fig. 6c. The shape of the damage site is a semi-sphere with clearly defined, sharp outer boundaries. The latter are not correlated with any particular microstructure feature (e.g., grain boundary, chemical segregation, melt pool boundary). A link to a video of the rotating dataset is available in Supplementary Material C.

Damage development sequence

One interesting observation in Fig. 5 is the presence of a keyhole defect in the middle of grain 1. In fact, pre-existing keyholes were observed within about 50% of the corrosion sites examined, suggesting that they are likely initiation sites, yet not systematic. Their cup-like morphology could lead to preferential trapping of chloride ions. This resembles the effect of lack of fusion (LOF) defects in decreasing the corrosion resistance of DED 304L alloy by Melia et al.[26].

Representative examples of corrosion damage are shown in Fig. 7 at different growth stages, from most to least mature. Figure 7a shows a fully developed damage site with equiaxed shape, resembling Fig. 6. Figure 7 on the other hand, shows a relatively less developed site, which clearly shows corrosion damage initiating around the keyhole before growing into the microstructure. Finally, Fig. 7c, d shows a top-down and cross-section view of a keyhole defect with incipient corrosion damage, developing at its rim. The focus ion beam (FIB) cross-section in Fig. 7d reveals that damage develops simultaneously laterally (i.e., on the surface) and in the bulk, under the form of protrusions. Together, these observations indicate that corrosion damage develops from a specific entry point onwards, expanding in a concentric manner. However, combined time-resolved and 3D characterization are needed to fully understand the development sequence of such peculiar morphology. Nevertheless, the large size of fully developed sites indicates a sustained driving force for their continued growth after reaching the breakdown potential.

Sub-cell scale driving forces to damage development

As mentioned earlier, the proximity of phases or domains with different composition or structure can result in selective dissolution of the phase with the lowest corrosion resistance. The chemical composition across the cellular structures was examined using scanning transmission electron microscopy energy dispersive spectroscopy (STEM-EDS), shown in Fig. 8a, b. The line profile in Fig. 8c reveals that the cell boundaries are enriched in nickel, chromium, and molybdenum, which is characteristic of the austenite-to-ferrite solidification mode traditionally observed in DED AM 316L[7,27]. The presence of the passivating elements (Cr and Mo) increases the corrosion resistance of the cell boundaries versus the cell interiors, which can explain their resistance to dissolution during anodic polarization.

While the cell interiors still contain a sufficient percentage of chromium to be considered "stainless"—about 18 wt% according to Fig. 8c—the cell walls are significantly enriched in both chromium and molybdenum, both of which are strong passive film stabilizers in chloride-containing environments. This results in the formation of a relatively more stable native passive film over the cell boundaries[28]. Li et al.[29] reported the formation of a thicker oxide film over the cell boundaries than within the cell interiors, during anodization of selective laser melted (SLM) 316L samples, over a wide range of potentials. This behavior is promoted by the higher Cr and Mo concentration, leading to improved corrosion resistance. Li et al.'s samples were produced using a different AM process and their electrochemical results were also collected in a different solution (0.5 M H_2SO_4 + 1.0 M MeOH) than the one used here and showed no difference in the pitting potential of the AM 316L versus its wrought counterpart. This was despite a lower corrosion current density and a higher corrosion potential in the AM sample, which shows the potential of this manufacturing process in enhancing corrosion performance of the 316L alloy in various environments. Beyond cellular segregation, Fig. 8b also reveals Mn-rich inclusions, primarily located on the cell walls. While these were postulated as initiation points in 316L by Tian et al.[8], the morphology of localized corrosion observed here indicates that the cell walls are systematically preserved, across all the sites observed in. In other words, the high Cr and Mo concentration in the cell walls overcomes any potential adversarial effect and preserves the cell walls. The lower concentration of Cr/Mo within the cell interiors leads to their selective dissolution, even if possibly started at any of these inclusions.

The electrochemical potential of the cell structures was mapped via correlated atomic force microscopy (AFM) and scanning Kelvin probe force microscopy (SKPFM), shown in Fig. 9. The cell walls have a higher potential

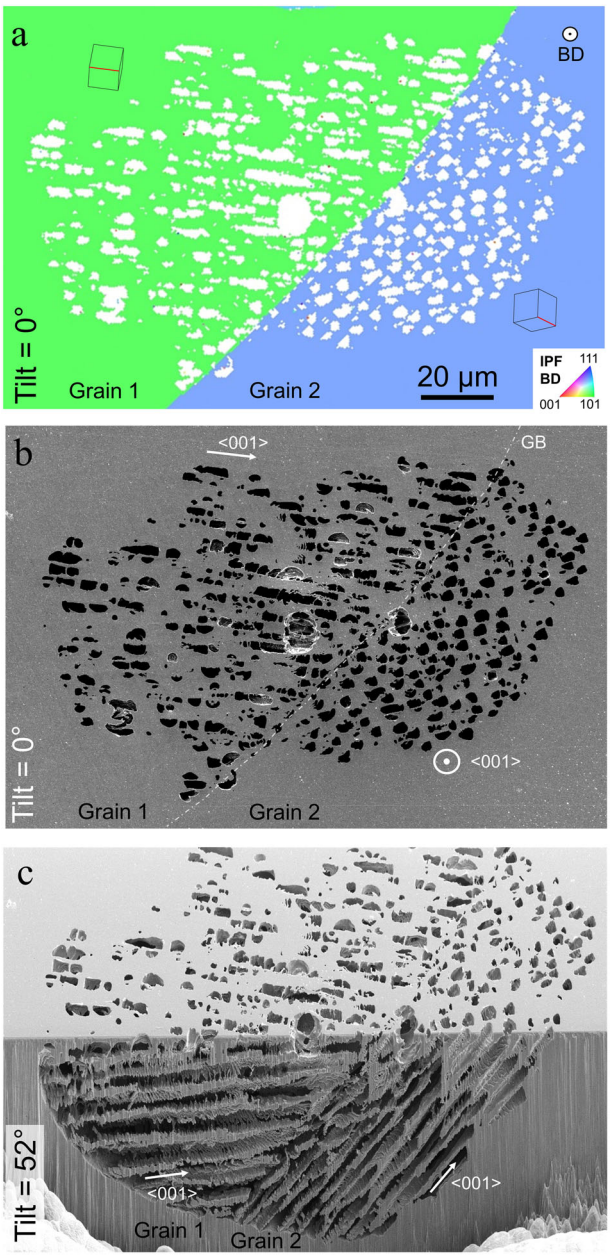

Fig. 5 | Crystallographic directionality of corrosion damage in AM 316L. a IPF-colored EBSD maps, with respect to the normal direction to the surface. Non-indexed points, corresponding to missing material, are colored in white. The local orientation of the cubic lattice is drawn in each grain, showing which crystallographic orientation is the closest to the directionality of the cavities; **b** corresponding SEM image showing clear correlation between cavities and local crystallographic orientation. Projections of the ⟨001⟩ directions, extracted from (**a**), are plotted with white arrows in each grain. The grain boundary is highlighted with light gray dashed lines; **c** corresponding cross-sectional view after FIB cutting, tilted to 52°, revealing the sub-surface structure of the damage site, ⟨001⟩ crystallographic directions projected from (**a**) are highlighted in both grains. The scale bar in (**a**) applies to (**b**, **c**).

of about 4 mV compared to their interior, in accordance with a higher percentage of noble elements. This difference in potential is similar to previously reported values in AM 316L[6,15,23], but rather small to consider micro-galvanic corrosion as the dominant mechanism[30]. Together, these measurements suggest that selective dissolution is likely the main driving force to localized corrosion, possibly accompanied by micro-galvanic effects.

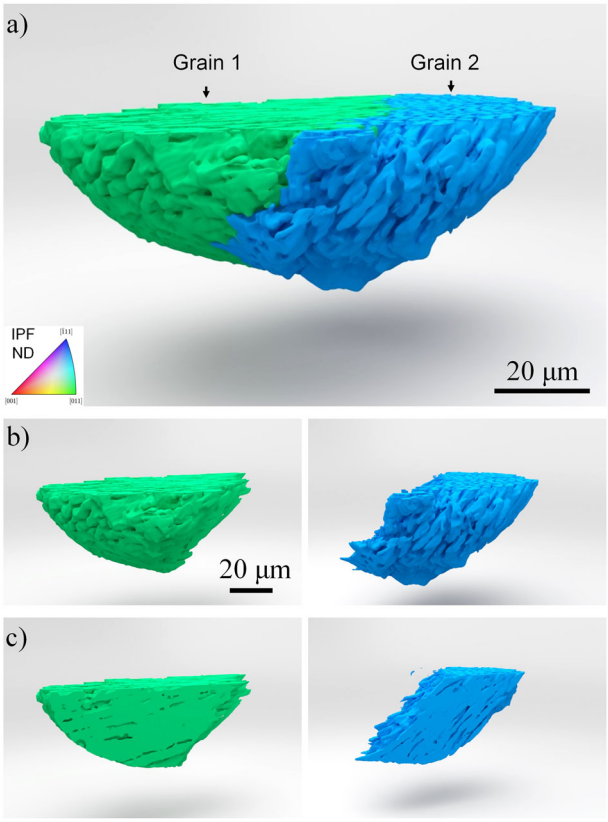

Fig. 6 | 3D reconstruction of the corrosion site shown in Fig. 5, after stacking all segmented slices. The volume rendered corresponds to the extruded material due to corrosion damage. All datasets shown in this figure, even though they correspond to "missing" material, are colored according to the local IPF colors with respect to the build direction (normal to the sample's surface), in accordance with Figs. 1 and 5. **a** 3D view of the full damage site, **b** split view of the damage in grains 1 and 2, **c** cross-sectional split view.

Discussion

Additive manufacturing introduces unique microstructural features that can be engineered with unprecedented control. The localized energy input during the process leads to rapid solidification, contributing to the formation of sub-grain structures that often result in improved mechanical properties[9]. The relationship between the microstructure and corrosion behavior of AM alloys is intricate and pivotal for determining the performance of the material in corrosive environments, however, overlooked at times when designing structural alloys. The microstructural features, including grain size, orientation, and the presence of printing defects, significantly influence the susceptibility of the alloy to corrosion. The segregation of crucial elements, such as chromium and molybdenum, can result in depleted regions with higher susceptibility to corrosion. The role of cell structures remains unclear. For instance, while the results reported by Revilla et al.[23] show a similar trend to ours, Tian et al.[8] observed the complete opposite behavior with selective dissolution of the cell walls. As observed in EDS results in Fig. 8c, the variation of Cr and Mo concentration from 20 to 18 wt% and 5 to 3.5 wt% from the cell wall to the interior causes the selective dissolution of the cell area, however, the initiation of the localized corrosion might be governed by the presence of printing defects, in this case, the keyholes.

In addition to defects, the presence of other heterogeneities, such as inclusions[8], carbides[31], or Cr/Mn/Mo-rich precipitates[32] within the cell boundaries can affect localized corrosion. Tian et al.[8] reported that Mn-rich silicates present on the cell walls are likely initiation sites for localized corrosion in LPBF 316L. While our STEM-EDS map presented in Fig. 8b also reveals the presence of Mn-rich precipitates on the cell walls, we did not find

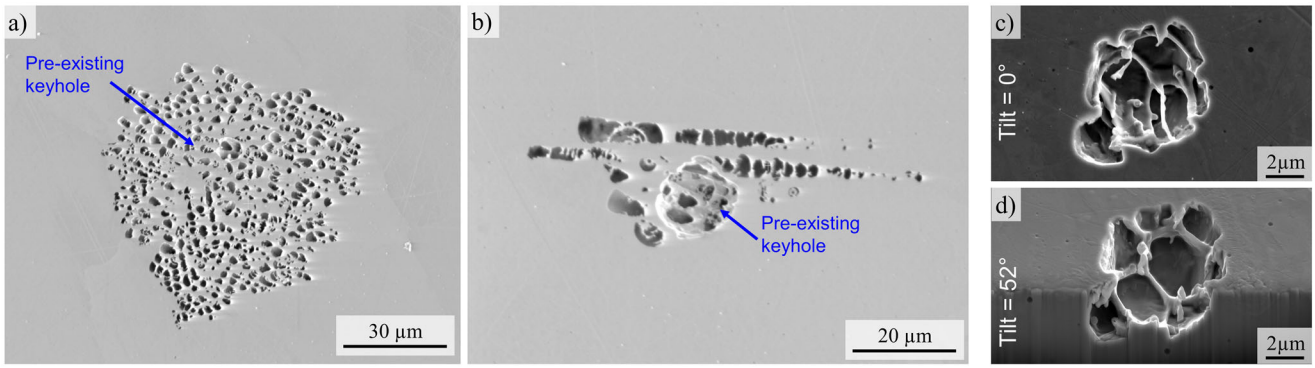

Fig. 7 | SEM micrographs of keyhole-induced corrosion damage. a Fully developed site, (**b**) partially developed site, (**c**, **d**) incipient site, (**d**) shows a FIB cross-section of (**c**) tilted to 52°.

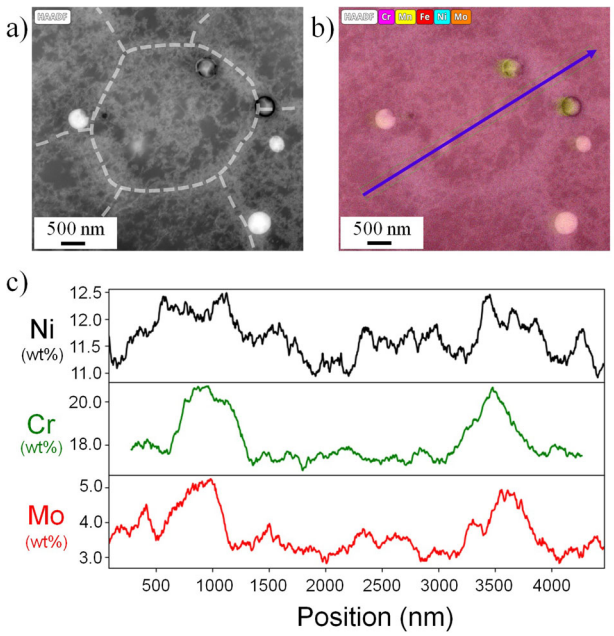

Fig. 8 | Segregation profile at the sub-cell scale. a STEM high-angle annular dark field (HAADF) image around a cell, showing dislocations and chemical segregation at its walls, **b** corresponding EDS map, with overlapped contributions of Fe, Ni, Cr, Mn and Mo, **c** Ni, Cr and Mo profiles along the blue arrow from (**b**).

any evidence of these precipitates playing a significant role in the subsequent stages of corrosion. In fact, Tian et al.[8] report preferential dissolution of the cell walls, starting from Mn-rich silicates whereas here, we report the opposite. While these precipitates are located on the cell walls, the latter are entirely preserved after PDP, which indicates that they may not affect localized corrosion in a significant manner.

One of the other influencing factors is the higher dislocation density at the cellular grain boundaries[5,8,32]. All these factors work opposite to the effect of Cr and Mo segregation in increasing the corrosion resistance of the cellular boundaries. Specifically, the results by Tian et al.[8] observed in both in situ TEM and bulk corrosion experiments with AM 316L showed the spread of corrosion attack along the dislocation network within the cell boundaries, highlighting the dominant role of dislocations against Cr/Mo segregation in LPBF 316L. While the presence of a high density of dislocations can be presumed to have a deteriorating effect on the protective properties of the passive film formed over the cellular boundaries, one would expect the higher concentration of Cr/Mo to counterbalance this effect. The balance between the two remains to be systematically investigated and quantified.

In fact, the presence of a keyhole in grain 1 in Fig. 5, suggests that damage likely started from this specific location and then expanded through grain 2, despite the presence of the grain boundary. It is unclear, however, whether the structure developed through or underneath the surface, whether its growth kinetics depend on the crystallographic orientation, or whether they are affected by the presence of the grain boundary.

In light of the preferential dissolution within cellular solidification structures, several solutions can be explored. First, post-build annealing treatments can be implemented, as explored by Chen et al.[2], who revealed a two-fold increase in breakdown potential as well as much smaller corrosion damage sites after homogenization of the cellular structures in DED 316L. Second, modifying the cellular structures—either the dislocation structures or the segregation in the cell walls—in a method similar to that employed by Seita et al.[33], would disrupt the driving force to damage growth. Vukkum et al.[11] observed an increase in the stability of the passive film via addition of CrN particles to the 316L feedstock. The solubility of the particles in the 316L matrix dynamically alters the chemical composition of the alloy as it is being printed, as well as its final microstructure, resulting in reduced damage and a higher pitting potential. Finally, the nature and amount of segregation at the cell walls could be engineered by tailoring the solidification pathway using thermodynamic calculations. This pathway has yet to be explored.

Methods

Gas atomized 316L stainless steel powder with diameter in the 45 µm–105 µm range and with nominal composition (in wt%) Fe-17.6%Cr-12.6%Ni-0.89%Mn-2.43%Mo-0.67%Si-0.019%C-0.02%O-0.007%P-0.004%S-0.09%N was purchased from Carpenter Technologies. Cylindrical specimens measuring 12 mm (diameter) × 76 mm (height) were built on a low carbon steel plate using a FormAlloy-L2 direct energy deposition (DED) system with a 1kW Nd:YAG laser (wavelength 1070 nm) and Gaussian energy profile. Argon was used for both the shielding and carrier gas for powder delivery. Printing was carried out using a laser power of 500 W, a scan speed of 1100 mm/s, and using a scan rotation of 90° between adjacent layers. Built samples were removed from the base plate using a band saw and cut using wire electrical discharge machining into 2 mm-thick disks. Fully recrystallized 316L was used as a baseline material. Recrystallized and AM samples were mechanically ground with SiC abrasive papers and polished using diamond suspensions, alumina suspensions, and colloidal silica with diameter down to 0.05 µm.

Potentiodynamic polarization

Potentiodynamic polarization (PDP) experiments were carried out using a VersaSTAT 3 Potentiostat from Princeton Scientific, which consists of a three-electrode cell configuration involving the alloy specimen as a working electrode, a Pt counter electrode, and a saturated Ag/AgCl reference electrode. The electrolyte used was a 0.6 M NaCl solution. PDP scans were performed in the anodic direction at a rate of 20 mV/min starting $-0.1V$

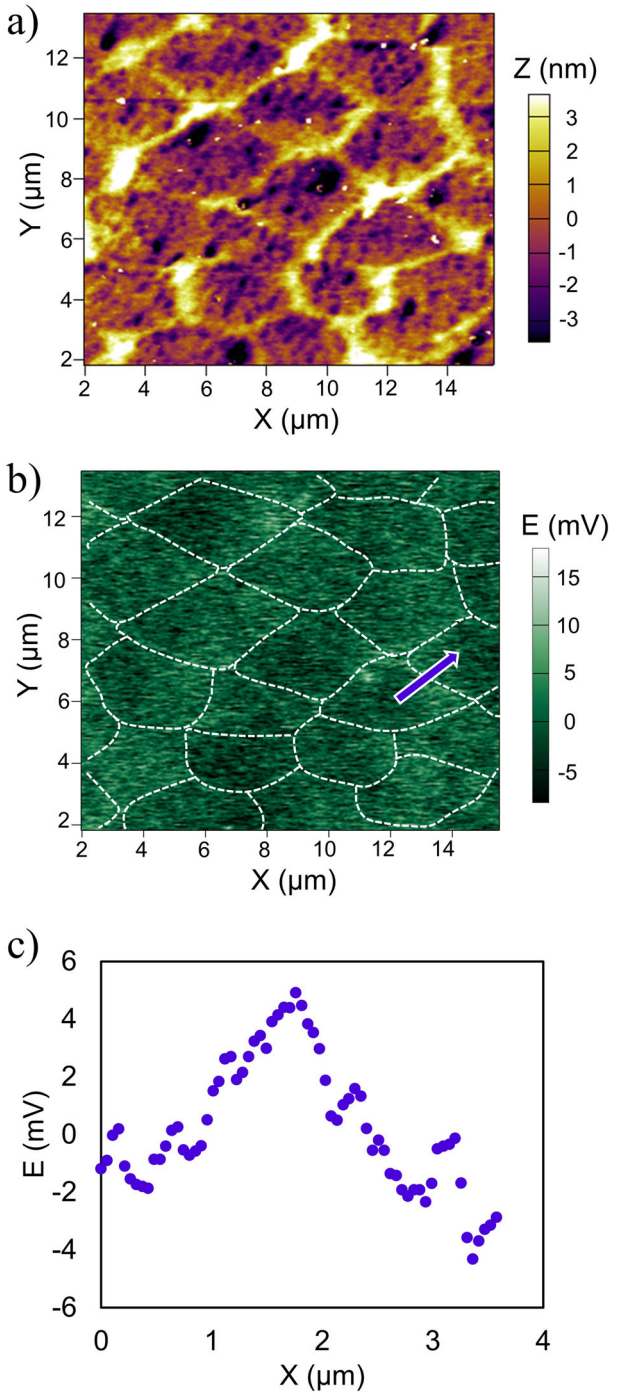

Fig. 9 | Electrochemical characterization of the cell structures in DED AM 316L. AFM mapping of the cellular structure in AM 316L: **a** topography map, **b** Volta potential map, and **c** variation of Volta potential across the cell boundary shown in (**b**).

below the open current potential (OCP), up to a potential exceeding the breakdown potential. For each specimen, at least three PDP curves were collected, to confirm the repeatability of the measurements. All specimens were inspected for crevice corrosion under an optical microscope after PDP testing, and only the specimens free of crevice corrosion were considered in the following.

Electron and atomic force microscopy

The microstructures of all specimens were characterized using a Thermo Fisher Scientific (TFS) Scios 2 scanning electron microscope (SEM) equipped with an Edax *Hikari Super* electron back-scatter diffraction (EBSD) camera under an acceleration voltage of 30 kV. A TFS Helios focused ion beam (FIB) SEM was used for serial sectioning and imaging. A sequence of cross-sectional micrographs were taken on a localized corrosion site on AM material following PDP. Micrographs were obtained using focused ion beam (FIB) milling on a TFS Helios 600i Dual Beam FIB-SEM. A total of 88 cross-sectional micrographs were recorded at intervals of 1 μm apart. Cross-sectional micrographs were then aligned and segmented into corroded and non-corroded regions using image processing. Stacked slices were used to create a 3D reconstruction of the corrosion damage site using the Avizo software. To characterize the dislocation structure and micro-segregation at the sub-cell level, twin-jet electro-polishing was employed to prepare electron-transparent foils from 70 μm thick samples, using an $HClO_4$ acid mix chilled down to −30 °C. A TFS Talos transmission electron microscope (TEM) equipped with a 4k × 4k *Ceta*^{TM} 16M camera and a *super-X* EDS system was operated at 200 kV to characterize the thin foils. AFM and SKPFM measurements were taken using an Asylum Research MFP-3D microscope. Conductive platinum coated AFM tip cantilevers (BudgetSensors) with resonant frequency of 75 khz and spring constant of 3N/m were used. AFM and SKPFM data was collected during a single scan with SKPFM being collected during re-pass.

Data availability

Data can be made available upon reasonable request.

Received: 14 February 2024; Accepted: 10 April 2024;
Published online: 30 April 2024

References

1. Nie, J., Wei, L., Jiang, Y., Li, Q. & Luo, H. Corrosion mechanism of additively manufactured 316l stainless steel in 3.5 wt.% nacl solution. *Mater. Today Commun.* **26**, 101648 (2021).
2. Chen, J. et al. Enhanced pitting resistance of directed energy deposition 316l stainless steel by post-manufacturing heat treatment. *npj Mater. Degred.* https://doi.org/10.1038/s41529-022-00237-1 (2022).
3. Lodhi, M., Deen, K. & Haider, W. Corrosion behavior of additively manufactured 316l stainless steel in acidic media. *Materialia* **2**, 111–121 (2018).
4. Vukkum, V. B. & Gupta, R. K. Review on corrosion performance of laser powder-bed fusion printed 316l stainless steel: effect of processing parameters, manufacturing defects, post-processing, feedstock, and microstructure. *Mater. Des.* **221** https://www.sciencedirect.com/science/article/pii/S0264127522004968 (2022).
5. Bertsch, K., de Bellefon, G. M., Kuehl, B. & Thoma, D. Origin of dislocation structures in an additively manufactured austenitic stainless steel 316l. *Acta Mater.* **199**, 19–33 (2020).
6. Kong, D. et al. About metastable cellular structure in additively manufactured austenitic stainless steels. *Addit. Manuf.* **38**, 101804 (2021).
7. Nie, Y., Chang, Y. & Charpagne, M. Functionally graded stainless steels with tailored grain boundary serration. *Scr. Mater.* **237**, 115714 (2023).
8. Tian, M., Choundraj, J. D., Voisin, T., Wang, Y. M. & Kacher, J. Discovering the nanoscale origins of localized corrosion in additive manufactured stainless steel 316l by liquid cell transmission electron microscopy. *Corros. Sci.* **208**, 110659 (2022).
9. Wang, Y. M. et al. Additively manufactured hierarchical stainless steels with high strength and ductility. *Nat. Mater.* **17**, 63–71 (2017).
10. Ettefagh, A. H., Guo, S. & Raush, J. Corrosion performance of additively manufactured stainless steel parts: a review. *Addit. Manuf.* **37**, 101689 (2021).
11. Vukkum, V. B., Christudasjustus, J., Darwish, A. A., Storck, S. M. & Gupta, R. Enhanced corrosion resistance of additively manufactured stainless steel by modification of feedstock. *npj Mater. Degrad.* https://doi.org/10.1038/s41529-021-00215-z (2021).

12. Sander, G. et al. On the corrosion and metastable pitting characteristics of 316l stainless steel produced by selective laser melting. *J. Electrochem. Soc.* **164**, C250–C257 (2017).
13. Ko, G., Kim, W., Kwon, K. & Lee, T.-K. The corrosion of stainless steel made by additive manufacturing: a review. *Metals* **11**, 516 (2021).
14. Voisin, T. et al. Pitting corrosion in 316l stainless steel fabricated by laser powder bed fusion additive manufacturing: a review and perspective. *JOM* **74**, 1668–1689 (2022).
15. Kong, D. et al. The passivity of selective laser melted 316l stainless steel. *Appl. Surf. Sci.* **504**, 144495 (2020).
16. Chao, Q. et al. On the enhanced corrosion resistance of a selective laser melted austenitic stainless steel. *Scr. Mater.* **141**, 94–98 (2017).
17. Ni, X.-Q et al. Anisotropy in mechanical properties and corrosion resistance of 316l stainless steel fabricated by selective laser melting. *Int. J. Miner. Metall. Mater.* **26**, 319–328 (2019).
18. Ryan, M. P., Williams, D. E., Chater, R. J., Hutton, B. M. & McPhail, D. S. Why stainless steel corrodes. *Nature* **415**, 770–774 (2002).
19. Sander, G. et al. Corrosion of additively manufactured alloys: a review. *Corrosion* **74**, 1318–1350 (2018).
20. Man, C. et al. The enhancement of microstructure on the passive and pitting behaviors of selective laser melting 316l ss in simulated body fluid. *Appl. Surf. Sci.* **467–468**, 193–205 (2019).
21. Meguid, E. A. A. E., Mahmoud, N. A. & Gouda, V. K. Pitting corrosion behaviour of AISI 316l steel in chloride containing solutions. *Br. Corros. J.* **33**, 42–48 (1998).
22. Vignal, V. et al. Pitting corrosion of type 316l stainless steel elaborated by the selective laser melting method: influence of microstructure. *J. Mater. Eng. Perform.* **30**, 5050–5058 (2021).
23. Revilla, R. I. et al. Microstructure and corrosion behavior of 316l stainless steel prepared using different additive manufacturing methods: a comparative study bringing insights into the impact of microstructure on their passivity. *Corros. Sci.* **176**, 108914 (2020).
24. Chen, Z. W., Phan, M. A. L. & Darvish, K. Grain growth during selective laser melting of a Co-Cr-Mo alloy. *J. Mater. Sci.* **52**, 7415–7427 (2017).
25. Farshidianfar, M. H., Khajepour, A. & Gerlich, A. P. Effect of real-time cooling rate on microstructure in laser additive manufacturing. *J. Mater. Process. Technol.* **231**, 468–478 (2016).
26. Melia, M. A., Nguyen, H.-D. A., Rodelas, J. M. & Schindelholz, E. J. Corrosion properties of 304l stainless steel made by directed energy deposition additive manufacturing. *Corros. Sci.* **152**, 20–30 (2019).
27. Smith, T. R., Sugar, J. D., Marchi, C. S. & Schoenung, J. M. Microstructural development in DED stainless steels: applying welding models to elucidate the impact of processing and alloy composition. *J. Mater. Sci.* **56**, 762–780 (2020).
28. Pardo, A. et al. Pitting corrosion behaviour of austenitic stainless steels—combining effects of Mn and Mo additions. *Corros. Sci.* **50**, 1796–1806 (2008).
29. Li, R. et al. Improved catalytic performance and corrosion resistance of selective laser melted 316L SS in a direct methanol fuel cell by surface anodization. *Surf. Coat. Technol.* **399**, 126172 (2020).
30. Liew, Y. et al. Towards understanding micro-galvanic activities in localised corrosion of aa2099 aluminium alloy. *Electrochim. Acta* **392**, 139005 (2021).
31. Raut, L. P., Taiwade, R. & Agarwal, A. Investigation of microstructural and corrosion behavior of 316lsi structure developed by wire arc additive manufacturing. *Mater. Today Commun.* **35**, 105596 (2023).
32. Barkia, B. et al. On the origin of the high tensile strength and ductility of additively manufactured 316l stainless steel: multiscale investigation. *J. Mater. Sci. Technol.* **41**, 209–218 (2020).
33. Gao, S. et al. Additive manufacturing of alloys with programmable microstructure and properties. *Nat. Commun.* **14** https://doi.org/10.1038/s41467-023-42326-y (2023).

Acknowledgements

E.D.V., T.L., Y.T.C. and M.A.C. acknowledge the Energy and Biosciences Institute via the EBI-Shell program (corrosion). Y.N. and M.A.C. gratefully acknowledge support from the National Science Foundation, CAREER award DMR-2236640 (synthesis, microstructure characterization, recrystallization). M.E. acknowledges the support from the Illinois Applied Research Institute. We acknowledge the use of facilities and instrumentation at the Materials Research Laboratory Central Research Facilities, University of Illinois. Finally we acknowledge the Imaging Technology Group at the Beckman Institute for their assistance with graphics, imaging, and videos in Fig. 6 and Supplementary Material.

Author contributions

E.D. and Y.N. designed the printing process and printed the samples. E.D. T.L. and M.E. performed the electrochemical tests, SEM, and data analysis. Y.T.C. collected the 3D dataset as well as the TEM data. E.D. collected and analyzed the AFM and SKPFM data. The manuscript was drafted by E.D. and revised by all the authors. M.A.C. conceptualized and supervised the work.

Competing interests

The authors declare no competing interests.

Additional information

Supplementary information The online version contains supplementary material available at https://doi.org/10.1038/s41529-024-00464-8.

Correspondence and requests for materials should be addressed to Marie A. Charpagne.